Published in final edited form as:
Inorg Chem. 2013 March 4; 52(5): 2627–2636. doi:10.1021/ic302543n.

Factors Influencing Conversion Kinetics of Triply-Bridged (μ-η^1:η^1-Peroxo)Diiron(III) Intermediates to Doubly-Bridged (μ-η^1:η^1-Peroxo)Diiron(III) Intermediates

Jonathan R. Frisch[†], **Ryan McDonnell**[‡], **Elena V. Rybak-Akimova**[‡,*], and **Lawrence Que Jr.**[*,†]

[†]Department of Chemistry and Center for Metals in Biocatalysis, University of Minnesota, 207 Pleasant St. S.E., Minneapolis, MN 55455

[‡]Department of Chemistry, Tufts University, 62 Talbot Ave., Medford, MA 02155

Abstract

Several $[Fe^{II}_2$(N-EtHPTB)(μ-O_2X)]$^{2+}$ complexes (**1**•O_2X) have been synthesized, where N-EtHPTB is the anion of *N,N,N′ N′*-tetrakis(2-benzimidazolylmethyl)-2-hydroxy-1,3-diaminopropane and O_2X is an oxyanion bridge. Crystal structures reveal five-coordinate (μ-alkoxo)diiron(II) cores. These diiron(II) complexes react with O_2 at low temperatures in CH_2Cl_2 (−90°) to form blue-green O_2 adducts that are best described as triply-bridged (μ-η^1:η^1-peroxo)diiron(III) species (**2**•O_2X). With one exception, all **2**•O_2X intermediates convert irreversibly to doubly-bridged, blue (μ-η^1:η^1-peroxo)diiron(III) species (**3**•O_2X). Where possible, **2**•O_2X and **3**•O_2X intermediates were characterized using resonance Raman spectroscopy, showing respective $\nu_{O\text{-}O}$ values of ~850 and ~900 cm^{-1}. How the steric and electronic properties of O_2X affect conversion of **2**•O_2X to **3**•O_2X was examined. Stopped-flow analysis reveals that oxygenation kinetics of **1**•O_2X are unaffected by the nature of O_2X and for the first time, the benzoate analog of **2**•O_2X (**2**•O_2CPh) is observed.

Introduction

Nonheme diiron enzymes have attracted great interest because they perform a wide variety of reactions despite having very similar active sites.[1–8] For example, soluble methane monooxygenase inserts an oxygen atom into an alkane C-H bond, toluene and *o*-xylene monooxygenases, as well as phenol hydroxylase insert oxygen atoms into aromatic C-H bonds, the R2 subunit of class I ribonucleotide reductases extracts a hydrogen atom producing a stable radical and, as its name implies, stearoyl acyl carrier protein Δ^9-desaturase dehydrogenates a fatty acid hydrocarbon chain. In addition to having similar active site structures, these enzymes all share one other property. The putative catalytic cycles of these enzymes all contain peroxide-bridged diiron(III) complexes formed upon reduction of molecular oxygen. In some cases, these intermediates are stable enough to be trapped and characterized.[9–17] While peroxo-diiron(III) species are endemic in these enzymes, their precise role in catalysis is poorly understood, even though they have been well studied. Synthetic attempts to study peroxo-diiron(III) intermediates have resulted in a variety of biomimetic complexes.[18–27] These compounds often form peroxide-bridged diiron(III) intermediates, especially when stabilized by carboxylate bridges. They are commonly reported as having a (μ-η^1:η^1-peroxo)diiron(III) motif.

[*]To whom correspondence should be addressed. elena.rybak-akimova@tufts.edu; larryque@umn.edu.

In a previous publication,[28] we discussed how replacing the carboxylate bridges commonly employed in synthesis of these biomimetic complexes affected the behavior of the peroxo intermediates formed. Using the dinucleating ligand N-EtHPTB (anion of *N,N,N′,N′*-tetrakis(2-benzimidazolylmethyl)-2-hydroxy-1,3-diaminopropane) combined with two equivalents of iron(II) and one equivalent of either benzoate, diphenylphosphinate or dimethylarsinate,[29] we demonstrated that two different (μ-η^1:η^1-peroxo)diiron(III) species can be formed upon reduction of dioxygen. A doubly-bridged (μ-alkoxo)(μ-1,2-peroxo) intermediate was obtained from the benzoate-bridged diiron(II) precursor at −40°, in contrast to the triply-bridged (μ-alkoxo)(μ-1,2-peroxo)(μ-1,3-dimethylarsinato) intermediate produced by the dimethylarsinate-bridged diiron(II) precursor. The diphenylphosphinate-bridged diiron(II) precursor was unique in that it formed a triply-bridged peroxo intermediate as the initial kinetic product, which converted to a metastable doubly-bridged peroxo intermediate by a shift of the phosphinate from a bridging mode to a terminal monodentate binding mode before peroxo decomposition, analogous to the "carboxylate shift" notion described by Lippard twenty years ago.[30] We concluded that the nature of the oxyanion bridge (O_2X) strongly influenced the nature and stability of any (μ-η^1:η^1-peroxo)diiron(III) species formed, but we felt further work was required before the effects of bridge differences could be clearly understood. This work is intended to address that issue.

To this end, we focused on three effects: *(i)* those produced by O_2X O···O bite distance differences, *(ii)* those produced by O_2X electronic differences and *(iii)* those produced by O_2X steric differences. Examination required synthesis of several new diiron(II) complexes (**1**•O_2X) using N-EtHPTB and various O_2X ligands. We found that all of these new species reacted with O_2 in solution to produce blue-green (μ-η^1:η^1-peroxo)diiron(III) intermediates (**2**•O_2X) at −90°. With one exception, they then converted to deep-blue (μ-η^1:η^1-peroxo)diiron(III) species (**3**•O_2X) before decaying to yellow products (**4**•O_2X) at higher temperature. In most cases, addition of $OPPh_3$ to solutions of **2**•O_2X led to conversion to purple-blue species (**3′**•O_2X) similar to **3**•O_2X. In this paper, we report crystallographic details of three diiron(II) complexes, kinetic data on their reactions with dioxygen, and spectroscopic characterization of a variety of (μ-η^1:η^1-peroxo)diiron(III) intermediates. Implications of O_2X bite distances as well as electronic and steric differences are discussed.

Experimental Section

Materials and Syntheses

All reagents and solvents were purchased from commercial sources and were used as received, unless noted otherwise. The ligand N-EtHPTB was synthesized using a published procedure.[31] Solvents were dried according to published procedures and distilled under Ar prior to use.[32] The $^{18}O_2$ (97%) used in resonance Raman experiments was purchased from Cambridge Isotope Laboratories, Inc., Andover, MA. Preparation and handling of air sensitive materials were carried out under an inert atmosphere by using either standard Schlenk and vacuum line techniques or a glovebox. Elemental analyses were performed by Atlantic Microlab, Inc., Norcross, GA.

1•O_2CPh, 1•O_2PPh_2 and 1•O_2AsMe_2 were synthesized using published procedures.[28]

1•O_2PMe_2—N-EtHPTB (157 mg, 0.217 mmol) was dissolved in MeOH (~10 mL) along with Et_3N (0.19 mL, 1.4 mmol). Dimethylphosphinic acid (21.6 mg, 0.230 mmol) was added and allowed to dissolve. $Fe(OTf)_2$•2MeCN[33] (189 mg, 0.434 mmol) was added, producing a yellow solution. After 5 minutes, $NaBPh_4$ (149 mg, 0.435 mmol) was added, resulting in immediate precipitation of a white powder. The solid was filtered and dried *in vacuo*. Recrystallization from MeCN and Et_2O produced colorless crystals, some suitable

for X-ray diffraction structural analysis. Yield: 153 mg (80%). Anal. for [Fe_2(N-EtHPTB)(O_2PMe_2)](BPh$_4$)(OTf) and calcd for $C_{70}H_{75}BF_3Fe_2N_{10}O_6PS$: C, 60.27; H, 5.42; N, 10.04%. Found: C, 59.82; H, 5.49; N, 10.38%.

1•$O_2P(OPh)_2$—N-EtHPTB (176 mg, 0.243 mmol) was dissolved in MeOH (~10 mL) along with Et3N (0.19 mL, 1.4 mmol). Diphenylphosphoric acid (67.7 mg, 0.271 mmol) was added and allowed to dissolve. Fe(OTf)$_2$•2MeCN (222 mg, 0.509 mmol) was added, producing a yellow solution. After 5 minutes, NaBPh$_4$ (173 mg, 0.506 mmol) was added, resulting in immediate precipitation of a white powder. The solid was filtered and dried *in vacuo*. Recrystallization from MeCN and Et_2O produced milky crystals, some suitable for X-ray diffraction structural analysis. Yield: 331 mg (79%). Anal. for [Fe_2(N-EtHPTB)($O_2P(OPh)_2$)](BPh$_4$)$_2$ and calcd for $C_{103}H_{99}B_2Fe_2N_{10}O_5P$: C, 71.87; H, 5.80; N, 8.14%. Found: C, 71.77; H, 5.94; N, 8.41%.

1•O_2CCPh_3—N-EtHPTB (208 mg, 0.288 mmol) was dissolved in MeOH (~10 mL) along with Et3N (0.19 mL, 1.4 mmol). Triphenylacetic acid (83.3 mg, 0.289 mmol) was added and allowed to dissolve. Fe(OTf)$_2$•2MeCN (257 mg, 0.589 mmol) was added, producing a yellow solution. After 5 minutes, NaBPh$_4$ (205 mg, 0.598 mmol) was added, resulting in immediate precipitation of a white powder. The solid was filtered and dried *in vacuo*. Recrystallization from MeCN and Et_2O produced colorless crystals. Yield: 370 mg (73%). Anal. for [Fe_2(N-EtHPTB)(O_2CCPh_3)](BPh$_4$)$_2$ and calcd for $C_{111}H_{104}B_2Fe_2N_{10}O_3$: C, 75.78; H, 5.96; N, 7.96%. Found: C, 75.46; H, 5.95; N, 7.96%.

1•O_2CCMe_3—N-EtHPTB (153 mg, 0.212 mmol) was dissolved in MeOH (~10 mL) along with Et_3N (0.19 mL, 1.4 mmol). Trimethylacetic acid (21.7 mg, 0.212 mmol) was added and allowed to dissolve. Fe(OTf)$_2$•2MeCN (186 mg, 0.426 mmol) was added, producing a yellow solution. After 5 minutes, NaBPh$_4$ (152 mg, 0.443 mmol) was added, resulting in immediate precipitation of a white powder. The solid was filtered and dried *in vacuo*. Recrystallization from MeCN and Et_2O produced milky crystals. Yield: 130 mg (50%). Anal. for [Fe_2(N-EtHPTB)(O_2CCMe_3)](OTf)$_2$ and calcd for $C_{50}H_{58}F_6Fe_2N_{10}O_9S_2$: C, 48.71; H, 4.74; N, 11.36%. Found: C, 48.91; H, 4.77; N, 11.39%.

1•$O_2CC_6H_2$-3,4,5-$(OMe)_3$—N-EtHPTB (72.9 mg, 0.101 mmol) was dissolved in MeOH (~10 mL) along with Et_3N (0.077 mL, 0.56 mmol). 3,4,5-Trimethoxybenzoic acid (21.4 mg, 0.101 mmol) was added and allowed to dissolve. Fe(OTf)$_2$•2MeCN (94.2 mg, 0.216 mmol) was added, producing a yellow solution. After 5 minutes, NaBPh$_4$ (87.2 mg, 0.255 mmol) was added, resulting in immediate precipitation of a pale yellow powder. The solid was filtered and dried *in vacuo*. Recrystallization from MeCN and Et_2O produced yellow crystals, some suitable for X-ray diffraction structural analysis. Yield: 116 mg (74%). Anal. for [Fe_2(N-EtHPTB)(O_2CCH_2-3,4,5-$(OMe)_3$)](BPh$_4$)(OTf) and calcd for $C_{78}H_{80}BF_3Fe_2N_{10}O_9S$: C, 61.92; H, 5.33; N, 9.26%. Found: C, 62.14; H, 5.55; N, 8.94%.

1•$O_2CC_6H_3$-3,4-$(OMe)_2$—N-EtHPTB (100.0 mg, 0.138 mmol) was dissolved in MeOH (~10 mL) along with Et_3N (0.097 mL, 0.69 mmol). 3,4-Dimethoxybenzoic acid (25.1 mg, 0.138 mmol) was added and allowed to dissolve. Fe(OTf)$_2$•2MeCN (120.3 mg, 0.276 mmol) was added, producing a yellow solution. After 5 minutes, NaBPh$_4$ (196.5 mg, 0.574 mmol) was added, resulting in immediate precipitation of a pale yellow powder. The solid was filtered and dried *in vacuo*. Recrystallization from MeCN and Et_2O produced milky crystals. Yield: 162 mg (89%). Anal. for [Fe_2(N-EtHPTB)($O_2CC_6H_3$-3,4-$(OMe)_2$)](OTf)$_2$ and calcd for $C_{54}H_{58}F_6Fe_2N_{10}O_{11}S_2$: C, 49.40; H, 4.45; N, 10.67%. Found: C, 49.65; H, 4.44; N, 10.39%.

1•$O_2CC_6H_3$-3,5-$(OMe)_2$—N-EtHPTB (146.1 mg, 0.202 mmol) was dissolved in MeOH (~10 mL) along with Et_3N (0.142 mL, 1.02 mmol). 3,5-Dimethoxybenzoic acid (37.0 mg, 0.203 mmol) was added and allowed to dissolve. $Fe(OTf)_2$•2MeCN (187.8 mg, 0.431 mmol) was added, producing a yellow solution. After 5 minutes, $NaBPh_4$ (190.6 mg, 0.557 mmol) was added, resulting in immediate precipitation of a pale green-yellow powder. The solid was filtered and dried *in vacuo*. Recrystallization from MeCN and Et_2O produced pale yellow crystals. Yield: 238.5 mg (80%). Anal. for $[Fe_2(\text{N-EtHPTB})(O_2CC_6H_3\text{-}3,5\text{-}(OMe)_2)](BPh_4)(OTf)_2$ and calcd for $C_{77}H_{78}BF_3Fe_2N_{10}O_8S$: C, 62.36; H, 5.30; N, 9.44%. Found: C, 62.56; H, 5.11; N, 9.33%.

1•$O_2CC_6H_4$-4-OMe—N-EtHPTB (149.2 mg, 0.206 mmol) was dissolved in MeOH (~10 mL) along with Et_3N (0.144 mL, 1.03 mmol). 4-Methoxybenzoic acid (31.3 mg, 0.206 mmol) was added and allowed to dissolve. $Fe(OTf)_2$•2MeCN (189.2 mg, 0.433 mmol) was added, producing a yellow solution. After 5 minutes, $NaBPh_4$ (205.4 mg, 0.600 mmol) was added, resulting in immediate precipitation of a pale green-yellow powder. The solid was filtered and dried *in vacuo*. Recrystallization from MeCN and Et_2O produced milky crystals. Yield: 245.4 mg (93%). Anal. for $[Fe_2(\text{N-EtHPTB})(O_2CC_6H_4\text{-}4\text{-}OMe)](OTf)_2$ and calcd for $C_{53}H_{56}F_6Fe_2N_{10}O_{10}S_2$: C, 49.62; H, 4.40; N, 10.92%. Found: C, 49.41; H, 4.51; N, 11.08%.

Physical Methods

UV-Vis spectra were recorded on a Hewlett-Packard 8453 diode array spectrophotometer (2-nm resolution) equipped with an Unisoku Scientific Instruments cryostat (Osaka, Japan). Resonance Raman spectra were collected on an ACTON AM-506M3 monochromator with a Princeton LN/CCD data collection system using a Spectra-Physics Model 2060 krypton laser. Low-temperature spectra of the peroxo intermediates in CH_2Cl_2 and MeCN were obtained at 77 K using a 135° backscattering geometry. Samples were frozen onto a gold-plated copper cold finger in thermal contact with a Dewar flask containing liquid nitrogen. Raman frequencies were referenced to the features of indene. Slits were set for a band-pass of 4 cm^{-1} for all spectra.

Time-resolved spectra of rapid oxygenation reactions were acquired with a Hi-Tech Scientific (Salisbury, Wiltshire, UK) SF-43 multi-mixing anaerobic cryogenic stopped-flow instrument combined with either a monochromator (low intensity light irradiation of the sample) or a diode array rapid scanning unit (strong UV-Vis irradiation of the sample), or with a TgK Scientific (formerly HiTech Scientific, Salisbury, Wiltshire, UK) SF-61DX2 cryogenic stopped-flow system equipped with a J&M Diode array (Spectralytics). All manipulations with diiron(II) complexes and their solutions were done using an argon atmosphere glove-box, air-tight syringes, and the anaerobic stopped-flow instrument to avoid contamination with air. Saturated solutions of O_2 in CH_2Cl_2 and CH_3CN were prepared by bubbling the dry O_2 gas for 20 min in a septum-closed cylinder with the solvent at a constant temperature (20 or 25 °C). The solubility of O_2 was accepted to be 5.8 mM in dichloromethane at 20° and 8.1 mM in acetonitrile at 25°.[34] Solutions of O_2 with smaller concentrations were prepared by diluting the saturated O_2 solution with argon-saturated solvent using graduated gas-tight syringes equipped with three-way valves. For the kinetic experiments, dioxygen was always taken in large excess so that its concentration did not change significantly during the reaction with **1**•O_2X. The solutions of **1**•O_2X and O_2 were cooled to a preset temperature (±0.1°) in the stopped-flow instrument before mixing. Data analysis was performed with the IS-2 Rapid Kinetics Software (Hi-Tech Scientific) for kinetic traces at a single wavelength.

X-ray Crystallography—X-ray diffraction data were collected on a Bruker SMART platform CCD diffractometer at 173(2) K.[35] Preliminary sets of cell constants were calculated from reflections harvested from three sets of 20 frames. These initial sets of frames were oriented such that orthogonal wedges of reciprocal space were surveyed. The data collection was carried out using MoKα radiation (graphite monochromator). Randomly oriented regions of reciprocal space were surveyed to the extent of one sphere and to a resolution of 0.84 Å. The intensity data were corrected for absorption and decay using SADABS.[36] Final cell constants were calculated after integration with SAINT.[37] The structures were solved and refined using SHELXL-97.[38] The space groups $P2_1/c$, $P2_1/n$ and $P\bar{1}$ were determined based on systematic absences and intensity statistics. Direct-methods solutions were calculated which provided most non-hydrogen atoms from the E-map. Full-matrix least squares/difference Fourier cycles were performed which located the remaining non-hydrogen atoms. All non-hydrogen atoms were refined with anisotropic displacement parameters. All hydrogen atoms were placed in ideal positions and refined as riding atoms with relative isotropic displacement parameters. The SQUEEZE function of the program PLATON[39] was used to remove 143 effective electrons in diffuse scattering from a volume of 1555.2 $Å^3$ per cell of **1**•$O_2P(OPh)_2(BPh_4)_2$•MeCN and 120 effective electrons in diffuse scattering from a volume of 1097.4 $Å^3$ per cell of (**1**•$O_2CC_6H_2$-3,4,5-$(OMe)_3)_2(BPh_4)_2(OTf)_2$•2MeCN. Brief crystal data and intensity collection parameters for the crystalline complexes are shown in Table 1.

Results

X-ray Crystallography

For this work, we synthesized diiron(II) complexes using a variety of O_2X ligands, namely O_2PMe_2, $O_2P(OPh)_2$, and several aliphatic and aromatic carboxylates, to augment a list that includes O_2AsMe_2, O_2PPh_2, and benzoate. We were able to obtain crystal structures of three of these **1**•O_2X compounds (O_2X = O_2PMe_2, $O_2P(OPh)_2$ and $O_2CC_6H_2$-3,4,5-$(OMe)_3$) (Table 2). Like those of previously published complexes,[28] the new complexes possess two distorted trigonal bipyramidal iron(II) centers, with N-EtHPTB amine nitrogen atoms and oxygen atoms from the bridging O_2X moiety occupying the axial positions. The equatorial sites are occupied by two benzimidazole nitrogen atoms and the alkoxide oxygen atom (Figure 1). With few exceptions, the respective atoms in the first coordination sphere of each complex reflect approximately equal interatomic distances and angles. Differences of note include average τ values,[40] O_2X bite distances, O-X-O angles and inter-iron distances. The τ values can be grouped into two sets with τ_{ave} ~ 0.8 (O_2X = O_2AsMe_2, O_2PPh_2 and O_2PMe_2) and τ_{ave} ~ 0.9 (O_2X = $O_2P(OPh)_2$, $O_2CC_6H_2$-3,4,5-$(OMe)_3$ and O_2CPh). Comparing bite distances of all complexes, we see O···O distances of ~2.55 Å (X = P) and ~2.23 Å (X = C). The lone X = As complex is in a class of its own with a bite distance of ~2.80 Å. It is also apparent that the O-X-O angle varies with the identity of the X atom (X = As, 113.26 deg.; X = P, 115.17 to 119.47 deg.; X = C, 123.4 to 124.2 deg.). The O-X-O angle measurement correlates inversely with O_2X bite distance; the species with the longest O···O distance (**1**•O_2AsMe_2) has the most acute O-X-O angle, while the X = C complexes have the shortest bite distances and largest O-X-O angles, with the X = P compounds falling in between these extremes. This inverse correlation reflects variations in X-O bond lengths ($As\text{-}O_{ave}$ = 1.676 Å; $P\text{-}O_{ave}$ = 1.501 Å; $C\text{-}O_{ave}$ = 1.261 Å. Even though the O-X-O angle decreases, concomitant lengthening of the X-O bonds results in a greater O···O distance.

In four of the six diferrous complexes crystallographically characterized, increased bite distance correlates to increased Fe···Fe distance. With the other two complexes, we observed that: *(i)* **1**•O_2AsMe_2 has an O···O distance ~0.24 Å longer than any other complex, although its interiron distance is within 0.01 Å of those found in both **1**•O_2PPh_2 and **1**•O_2PMe_2. *(ii)*

1•$O_2P(OPh)_2$ has an O···O distance on par with **1**•O_2PPh_2 and **1**•O_2PMe_2, yet its interiron distance (3.6211 Å) is the greatest of all the compounds, exceeding the distances found in **1**•O_2AsMe_2 (3.5357 Å) and the two other X = P species (3.5405 and 3.5364 Å) by ~0.08 Å. This is greater than the ~0.06 Å difference observed between the Fe···Fe distances of the X = C complexes (3.4879 and 3.4749 Å) and those with Fe···Fe distances of ~3.54 Å. The unusually long Fe···Fe distance in **1**•$O_2P(OPh)_2$ is most likely not due to packing effects, because a similar interiron distance of 3.649 Å was reported when **1**•$O_2P(OPh)_2$ crystallized in a different space group (P-1) with different anions (ClO_4).[41]

There are two crystallographically interesting observations regarding the compounds we report here and those examined in our previous work.[28] First, we note that [Fe_2(N-EtHPTB)(O_2PMe_2)](BPh_4)(OTf)(MeCN) and [Fe_2(N-EtHPTB)(O_2AsMe_2)](BPh_4)(OTf)(MeCN) are crystallographically isostructural. Both fall into the space group $P2_1/c$ with Z = 4 and share virtually identical unit cells with respective values for a, b and c of 16.0709(9) vs. 16.1151(12), 15.6360(9) vs. 15.7370(12) and 28.4703(15) vs. 28.473(2) Å. The α and γ angles are exactly 90 degrees and the β angles are respectively 103.5800(10) and 103.4900(10) degrees. The respective cations, anions and solvent molecules in each unit cell lie in essentially the same positions with the same orientations. The minor variations in unit cell parameters and atom positions arise from differences around the X atom of the O_2X bridging moieties. Small angle changes around X as well as X-C and X-O bond length variations produce minor differences in the cations which slightly alter the position of every other atom in the unit cell due to packing effects. The second observation is that the unit cell containing the cation [Fe_2(N-EtHPTB)($O_2CC_6H_2$-3,4,5-$(OMe)_3$)]$^{2+}$ contains a pseudo-inversion center lying between cations (Figure 2). This effectively doubles the number of unique elements per unit cell, thus doubling the size of the unit cell. The cation “inversion” is reasonably true, but the anions are farther away from the pseudo-inversion center, resulting in greater distortion during “inversion”. Because the differences between the cations are not significant, we chose to focus on one cation rather than redundantly discussing what essentially amounts to duplicate cations.

Observation of Two Peroxo Intermediates

Upon reaction with O_2, the virtually colorless solutions of **1**•O_2X produce blue-green O_2 adducts (**2**•O_2X), which in all cases except two convert to deep blue species (**3**•O_2X) before decaying to yellow final products (**4**•O_2X). Previously, we reported the formation of **2**•O_2PPh_2 and its conversion to **3**•O_2PPh_2 at −40°.[28] Corresponding studies with O_2X = benzoate afforded only evidence for the formation of **3**•O_2CPh under these conditions.[29,42,43] However, visible spectral evidence was obtained for the formation of both **2**•O_2CR and **3**•O_2CR by going to −90° in CH_2Cl_2, as shown in Figure 3 for O_2X = O_2CCPh_3 with respective λ_{max} values at 708 and 630 nm. In general, the visible chromophores of **2**•O_2X and **3**•O_2X fall in the ranges of 630–710 and 580–620 nm, respectively (Table 3), which have been previously assigned to peroxo-to-iron(III) charge transfer transitions for O_2X = benzoate, Ph_2PO_2, and Me_2AsO_2 by resonance Raman spectroscopy.[28,42]

Resonance Raman spectra for **2**•O_2CCPh_3, **3**•O_2CCPh_3, **2**•$O_2P(OPh)_2$, and **3**•$O_2P(OPh)_2$ shown in Figure 4 are representative of the species observed in this study. $^{16}O_2$ and $^{18}O_2$ labeling experiments reveal O-O stretching frequencies (Table 4) that by comparison to those previously published[28,42] allow us to sort them into two clusters. The **2**•O_2X cluster exhibits $\nu_{O\text{-}O}$ values ranging from 839 to 851 cm^{-1} that downshift to 791–807 cm^{-1} upon ^{18}O substitution, while the **3**•O_2X cluster has $\nu_{O\text{-}O}$ values ranging from 897 to ~910 cm^{-1} that downshift to 845–857 cm^{-1} with ^{18}O incorporation. On the other hand, no systematic difference is observed for the $\nu_{Fe\text{-}O}$ values of the **2**•O_2X and **3**•O_2X complexes,

all of which range from 457 to 479 cm^{-1} (Table 4). These features can be assigned to the symmetric Fe-O stretch of the Fe–O_2-Fe moiety and often appear as Fermi doublets. The difference in the $\nu_{O\text{-}O}$ values of **2**•O_2X and **3**•O_2X complexes has previously been attributed to a change in the Fe–Fe distance in the O_2 adducts on the basis of a systematic study of 1,2-peroxo-bridged diiron(III) complexes by Fiedler *et al.*[27] For the **2**•O_2X and **3**•O_2X complexes, the change in the Fe-Fe distance indicated by the difference in the $\nu_{O\text{-}O}$ values is postulated to derive from the conversion of the O_2X moiety from a bidentate bridging ligand in **2**•O_2X to a terminal monodentate ligand in **3**•O_2X (Scheme 1).

Attempts to obtain resonance Raman spectra for either **2**•$O_2CC_6H_2$-3,4,5-$(OMe)_3$ or **2**•$O_2CC_6H_3$-3,4-$(OMe)_2$ were unsuccessful, even though they exhibited a longer half life than **2**•O_2CCPh_3. A color change was observed during the freezing process. Their respective Raman spectra were comparable to those of **3**•$O_2CC_6H_2$-3,4,5-$(OMe)_3$ and **3**•$O_2CC_6H_3$-3,4-$(OMe)_2$, indicating conversion took place during the phase change (Figure S1). On the other hand, the longer lifetimes of the **3**•O_2X intermediates allowed us to collect spectra of every one (Figures 4 and S1), with the exception of **3**•O_2PMe_2, which did not form in quantities sufficient for characterization. The resonance Raman spectrum of **3′**•O_2PPh_2, formed by treatment of **2**•O_2PPh_2 with an excess of $OPPh_3$ (Figure 5) was also acquired. As it was nearly identical to the previously reported spectrum of **3′**•O_2CPh,[27] we did not carry out the corresponding experiments with other **3′**•O_2X intermediates.

Conversion of 2•O_2X to 3•O_2X

The spectral differences between **2**•O_2X and **3**•O_2X make UV-Vis absorption spectroscopy an excellent tool for following the transition from the first peroxo intermediate to the second. Based on the data shown in Figure 3, analysis of the spectral changes observed upon oxygenation of **1**•O_2CCPh_3 at −90° afforded a first-order rate constant of 1.7×10^{-3} s^{-1} for the conversion of **2**•O_2CCPh_3 to **3**•O_2CCPh_3. This value is comparable to that previously reported for the conversion of **2**•O_2PPh_2 to **3**•O_2PPh_2 at −40°, thus implicating a more facile conversion for the carboxylate-bridged species. Figure 6 provides evidence for the formation of two peroxo species at −90° as well even for the well studied complex **1**•O_2CPh,[29,42,44] although they are not as spectroscopically distinct as those of **2**•O_2CCPh_3 and **3**•O_2CCPh_3. Stopped-flow kinetic analysis at −80°C revealed the conversion from **2**•O_2CPh to **3**•O_2CPh with a k_{obs} of 5.3×10^{-2} s^{-1}, much faster than that observed for **2**•O_2CCPh_3 to **3**•O_2CCPh_3 at −90°. This comparison provides a rationale for why **2**•O_2CPh was not observed previously.[29,42,44] The rate of conversion of **2**•O_2X to **3**•O_2X decreased as electron donating substituents were introduced onto the benzoate ring or as the steric bulk of the carboxylate bridge was increased (Table 5). The rate of conversion was further decreased by replacing the trigonal carboxylate moiety with tetrahedral anions such as $(PhO)_2PO_2^-$, $Ph_2PO_2^-$, $Me_2PO_2^-$, and $Me_2AsO_2^-$ (Table 5).

In our previous publication,[28] we postulated that the conversion of **2**•O_2X to **3**•O_2X in acetonitrile involves a change in O_2X binding mode from bridging to terminal and coordination of a solvent molecule in position L (Scheme 1). For this work we added $OPPh_3$ to solutions of **2**•O_2X in hopes of substituting it into the L position. Upon $OPPh_3$ addition, purple-blue species (**3′**•O_2X) indeed form with λ_{max} values at wavelengths near each respective **3**•O_2X, although the extinction coefficients of the new intermediates are higher than those observed for each respective **3**•O_2X (Table 3) with the exception of the $O_2CC_6H_3$-3,4-$(OMe)_2$-based species. While facile conversion to **3′**•O_2X from most **2**•O_2X intermediates was accomplished by adding 20 equivalents of $OPPh_3$ at −90°, **2**•O_2PMe_2 and **2**•O_2PPh_2 had to be warmed to −40° to attain reasonable rates of conversion. In contrast, **2**•O_2AsMe_2 appears to be unaffected by addition of up to 100 equivalents of $OPPh_3$, even at temperatures as high as 20°.

After finding evidence indicating the formation of **2**•O_2CPh, we opted to further examine the oxygenation kinetics of both **1**•O_2PPh_2 and **1**•O_2CPh using stopped-flow techniques. **1**•O_2PPh_2 offers an excellent opportunity to characterize the initial oxygen coordination with the formation of **2**•O_2PPh_2, since the subsequent rearrangement of **2**•O_2PPh_2 to **3**•O_2PPh_2 is relatively slow. The reaction between **1**•O_2PPh_2 and O_2 in either MeCN or CH_2Cl_2, which is accompanied by rapid growth of the absorption band with $\lambda_{max} \approx 680$ nm, was studied. At low temperatures (down to −80 °C in CH_2Cl_2), the initially formed diiron-O_2 intermediate **2**•O_2PPh_2 is stable for at least an hour. However, noticeable decay of this intermediate was observed under intense illumination with polychromatic, UV-rich light of the arc lamp. In order to avoid complications from undesirable photodecomposition, quantitative kinetic measurements were performed in a single-wavelength mode, with low-intensity monochromatic light and a sensitive photomultiplier detector. Under these conditions, photobleaching was not observed. In order to determine the rate law, kinetic traces were acquired under large excess of O_2, showing single-exponential growth of **2**•O_2PPh_2 and yielding the values of observed pseudo-first-order rate constants, k_{obs}. The observed rate constants did not depend on the initial concentration of **1**•O_2PPh_2, in agreement with a rate law that is first-order in the diiron precursor. The observed rate constants increased linearly with an increase in the concentration of O_2 (Figure S3), indicating that the reaction was first order in dioxygen. It can be concluded that the formation of **2**•O_2PPh_2 is a second-order process (first-order in diiron complex and first-order in O_2): $v = k_2[\mathbf{1}\bullet O_2PPh_2][O_2]$

As temperature was raised, the oxygenation rate of **1**•O_2PPh_2 increased modestly, and the conversion of **2**•O_2PPh_2 to **3**•O_2PPh_2 became pronounced. The Eyring plot (Figure 7) for the oxygen binding step was linear over a broad temperature range (from −80 to −20° in CH_2Cl_2), yielding the activation parameters that are summarized in Table 6. Kinetics of oxygen binding to **1**•O_2PPh_2 in MeCN were also examined, and very similar activation parameters were extracted (Table 6). Subsequent disappearance of **2**•O_2PPh_2 was readily observed in MeCN at temperatures above −40 °C (Figure S4). The spectral changes agreed well with the conversion of **2**•O_2PPh_2 into **3**•O_2PPh_2 described in detail by Frisch *et al.*[28] Low activation enthalpies and large negative activation entropies for the oxygenation of **1**•O_2PPh_2 leading to **2**•O_2PPh_2 are typical of associative O_2 coordination at vacant or labile iron sites,[34,45] which are present in the starting diiron(II) complex. The rates and activation parameters for the oxygenation of **1**•O_2PPh_2 in CH_2Cl_2 or in acetonitrile are very similar to previously published kinetic parameters for the oxygenation of **1**•O_2CPh in propionitrile.[43] The kinetics of oxygenation of 5-coordinate diiron(II) complexes with a related dinucleating ligand HPTP are also very similar (Table 6).[46]

A closer examination of dioxygen binding to **1**•O_2CPh identified the individual reaction steps of the overall reaction. Stopped-flow observation of the reaction of **1**•O_2CPh with dioxygen (2.9 mM) in CH_2Cl_2 at −80° reveals a two-step process (Figure S5), in agreement with sequential formation of intermediates **2**•O_2CPh and **3**•O_2CPh. At longer wavelengths (greater than ca. 650 nm), the initial absorbance increase takes place within 15 seconds and is followed by decay that is complete within 100 seconds. At 640 nm, the initial absorbance increase was also seen, but after 15 seconds the kinetic trace becomes flat. At shorter wavelengths, a biexponential absorbance increase was seen. Two-exponential fit of the variable-wavelengths data gave the following value of the observed rate constant: $k_1 = 0.22$ s^{-1} at −80 °C (76 $M^{-1}s^{-1}$ under an assumption of a second-order process). This rate constant corresponds to the first reaction step, formation of **2**•O_2CPh. Interestingly, it is in excellent agreement with the reported value of the rate constant for the reaction of **1**•O_2CPh with O_2 (135 $M^{-1}s^{-1}$ at −75 C in propionitrile, with the activation parameters of $\Delta H^{\ddagger} = 15.4$ kJ/mol $\Delta S^{\ddagger} = -121$ J K^{-1} mol^{-1}).[43] In that work, **3**•O_2CPh was characterized spectroscopically,

and it was assumed that the kinetics of oxygenation corresponded to the formation of **3**•O_2CPh. Based on our studies, the kinetic parameters reported by Feig *et al.*[43] correspond to the first oxygenation step, the formation of **2**•O_2CPh; the next step, conversion of **2**•O_2CPh to **3**•O_2CPh, is very rapid at most temperatures.

Discussion

One step in the catalytic activation of dioxygen by biological diiron(II) systems often produces (μ-η^1:η^1-peroxo) diiron(III) moieties. Some of these intermediates exhibit a level of stability that allows for them to be trapped and characterized.[9–16] The same is true for many synthetic (μ-η^1:η^1-peroxo) diiron(III) complexes,[18,25,27,41,47] some of which are so stable they have been crystallographically characterized.[19–22] In previously published work,[28] we used the dinucleating ligand N-EtHPTB and different oxyanions (O_2X) to synthesize a set of three dioxygen binding diiron(II) complexes (**1**•O_2X). Our efforts revealed that the (μ-η^1:η^1-peroxo) diiron(III) intermediates produced upon oxygenation of the diiron(II) precursors come in two forms, green-blue **2**•O_2X and deep blue **3**•O_2X (Scheme 1). In the initial form, the oxyanion acts as a three-atom bridge between the iron centers and the pendant benzimidazoles are *cis* to each other on each iron. In many cases, this intermediate converts to a second form, wherein the O_2X ligand has moved to a terminal position, allowing the pendant benzimidazoles of the N-EtHPTB ligand to rearrange from a *cis* to a *trans* disposition on each iron. We found that the stability of **2**•O_2X is influenced by the identity of O_2X (O_2X = O_2AsMe_2, O_2PPh_2 and O_2CPh) and concluded that the dominant factor governing **2**•O_2X stability is the bite distance (O···O) of the O_2X moiety in **1**•O_2X as determined by X-ray crystallography. Anions with greater bite distances are better able to accommodate the >3 Å Fe···Fe distance in **2**•O_2X and gave rise to more stable 2•O_2X intermediates; for X = O_2AsMe_2, the **2**•O_2X intermediate was so stable that no observable conversion to **3**•O_2X was observed prior to decomposition.

For this work, we synthesized several more **1**•O_2X complexes to assess additional factors that may affect the stability of **2**•O_2X. Specifically, we were interested in examining effects produced by electronic and steric changes in O_2X and how those results relate to effects produced by differences in O_2X bite distances. We also investigated how $OPPh_3$ could be used to destabilize some **2**•O_2X intermediates. In addition, we used low-temperature stopped-flow techniques to demonstrate that the oxygenation of **1**•O_2CPh was in fact a two-step process like those we have described for the other **1**•O_2X complexes. Indeed, **2**•O_2CPh is short-lived even at −90°, so the adduct we originally observed at −40° and assigned to be **2**•O_2CPh in 1990[29,42] is in actuality the more stable **3**•O_2CPh isomer. Finally, we determined the activation parameters for the oxygenation of **1**•O_2PPh_2 in CH_2Cl_2 and in MeCN and found them to be very similar to those reported earlier for **1**•O_2CPh in EtCN (Table 6),[43] strongly suggesting a common rate determining step for these reactions corresponding to the formation of **2**•O_2X.

The focus of the experiments reported in this paper has been to gain further insight into the factors that affect the conversion of **2**•O_2X to **3**•O_2X, in which irreversible conversion to **3**•O_2X is preceded by movement of the O_2X moiety from a bridging to a terminal position (Scheme 1). We postulate that there is a rapid equilibrium between bridging and terminal coordination modes of the O_2X ligand in **2**•O_2X and only the isomer with a terminal O_2X ligand can undergo conversion to **3**•O_2X during which the benzimidazole arms of the N-EtHPTB ligand shift from a *cis* relationship to each other to a *trans* configuration on both iron centers. Thus the initial preequilibrium should be affected by the basicity of O_2X ligands, with the more basic ligand favoring the bridging mode and thereby decreasing the fraction of monodentate O_2X isomer available to undergo conversion to **3**•O_2X. On the other hand, as the transformation from **2**•O_2X to **3**•O_2X entails a significant rearrangement of the

coordination spheres about each iron center, the conversion should be slowed down by an increase in the steric bulk of O_2X.

The trend in the stability of the **2**•O_2X complexes is best discerned by an examination of the kinetic data for the large subset of complexes with carboxylate bridges. A perusal of Table 5 suggests that, while it may be possible to observe an effect of ligand basicity in comparisons of select pairs (e.g. O_2CPh vs. $O_2CC_6H_4$-4-OMe and O_2CPh vs. O_2CCMe_3), for the most part steric considerations supersede ligand basicity arguments. For example, the stability of **2**•O_2CR is enhanced 30-fold in the series, R = Ph < CMe_3 < CPh_3, commensurate with the increase in steric bulk on the carbon atom adjacent to the carboxylate function. Although the higher pK_a (5.03) of HO_2CCMe_3[48] relative to benzoic acid (pK_a = 4.19)[48] could be used to rationalize the threefold longer lifetime of **2**•O_2CCMe_3, the 30-fold greater stability of **2**•O_2CCPh_3 than **2**•O_2CPh cannot be explained by the slightly lower pK_a of HO_2CCPh_3 (3.96)[49] but can easily be rationalized by the much greater bulk of the triphenylmethyl group relative to phenyl.

Complexes with methoxy-substituted benzoate bridges support the above arguments. The conversion of **2**•$O_2CC_6H_2$-3,4,5-$(OMe)_3$ to its **3**•O_2X form is 100-fold slower that for **2**•O_2CPh, despite the fact that the two carboxylic acids have essentially identical pK_a values (4.24 and 4.19, respectively).[48,50] Therefore the considerable difference in the stabilities of **2**•$O_2CC_6H_2$-3,4,5-$(OMe)_3$ and **2**•O_2CPh (Table 5) must arise from steric considerations. Other methoxy-substituted benzoate complexes exhibit intermediate rates of conversion; **2**•$O_2CC_6H_3$-3,4-$(OMe)_2$ converts just slightly faster than **2**•$O_2CC_6H_2$-3,4,5-$(OMe)_3$, while **2**•$O_2CC_6H_3$-3,5-$(OMe)_2$ and **2**•$O_2CC_6H_4$-4-(OMe) are 10-fold faster. From these results, it seems clear that additional steric bulk in the *meta* and/or *para* positions of benzoate-based oxyanions is the primary factor that stabilizes the resultant **2**•O_2X complexes.

The lifetimes of **2**•O_2CR complexes are shortened upon addition of $OPPh_3$. We previously found that $OPPh_3$ had a good binding affinity for the parent $Fe^{III}{}_2$(N-Et-HPTB)-peroxo complex and exerted such a significant stabilizing effect that its presence led to the crystallization and structural characterization of [$Fe^{III}{}_3$(μ-1,2-O_2)(N-Et-HPTB)$(OPPh_3)_2$]$^{3+}$.[20] Addition of 20 equivalents of $OPPh_3$ to **2**•O_2CR at −90° in fact accelerated the conversion to **3′**•O_2CR with rates of 0.03–0.2 s^{-1}, representing a much smaller range of values than for the conversions in the absence of $OPPh_3$ (Table 5). These results suggest that the binding of $OPPh_3$ to the diiron center facilitates the ligand rearrangement required to convert from **2**•O_2X to **3**•O_2X (Scheme 1).

Tetrahedral O_2X bridges also increase the stability of **2**•O_2X. In this series, we compared complexes with O_2AsMe_2, O_2PMe_2, O_2PPh_2 and $O_2P(OPh)_2$ bridges that differ in steric properties and basicity (pK_a = 6.27, 3.08, 2.32 and 1.85, respectively).[51–53] The order of stability in this subset is O_2AsMe_2 > O_2PMe_2 > O_2PPh_2 > $O_2P(OPh)_2$ (Table 4), following the trend of decreasing pK_a values. Only **2**•$O_2P(OPh)_2$ undergoes conversion to the corresponding **3**•O_2X form at −90°, with k_{obs} = 1.2(1) × 10^{-4} s^{-1}, a rate that is slower than observed for five of the six **2**•O_2CR complexes at −90° (Table 5). While **2**•O_2PPh_2 is indefinitely stable at −90°, it converts to **3**•O_2PPh_2 when warmed to −40°, at a rate comparable to that of **2**•$O_2P(OPh)_2$ at −90°. Neither **2**•O_2PMe_2 nor **2**•O_2AsMe_2 generate an observable **3**•O_2X form; instead they appear to decay directly to **4**•O_2X. However, **2**•O_2PMe_2 can be converted to **3′**•O_2PMe_2 at −40° by addition of $OPPh_3$, whereas **2**•O_2AsMe_2 does not convert to **3′**•O_2AsMe_2, even when reacted with 100 equivalents of $OPPh_3$ at room temperature. The increasing stability of **2**•O_2X with the bite distance of the oxyanion bridge (X = C, 2.23 Å; X = P, 2.55 Å; X = As, 2.80 Å) reflects the ability of the O_2X bridge to span the Fe•••Fe distance required by the dinucleating HPTB ligand framework without imposing a strain on the six-member ring formed by the three atoms of

the oxyanion bridge, the two iron atoms and the alkoxide oxygen on the N-EtHPTB ligand. The O_2AsMe_2 complex, having the longest O•••O bite distance, represents the most stable of the **2**•O_2X intermediates.

In this paper, we have investigated the various factors that influence the conversion of **2**•O_2X O_2 adducts to corresponding **3**•O_2X species. This conversion entails the shift of the O_2X ligand from a bidentate bridging mode to a terminal monodentate mode, providing another example of a diiron complex involved in a mechanistically important "carboxylate shift" first recognized by Lippard and coworkers twenty years ago.[30] An analogous carboxylate shift has been suggested by Do *et al*.[54] to occur upon protonation of O_2 adducts of $[Fe^{II}_2$(N-EtHPTB)(μ-O_2CR)]$^{2+}$ complexes (R = Ph or C_6F_5) at −30°. However, although unequivocal evidence was provided for the protonation of the carboxylate ligand, it is clear from a comparison with the spectroscopic data we have presented in this paper that the O_2 adducts studied by Do *et al*.[54] must be assigned structures we now associate with **3**•O_2CR complexes, which have terminal monodentate carboxylates. On the other hand, the corresponding **2**•O_2CR complexes (with bridging carboxylates) are in fact formed upon oxygenation of the diiron(II) precursors (as previously assumed[29,42,54]) but can be observed only at −90°, as they readily undergo the "carboxylate shift" at that temperature to isomerize to corresponding **3**•O_2CR species. However, the key take-home message of the study by Do *et al*.[54] is that protonation of a carboxylate ligand on a diiron complex can occur and give rise to a complex with a carboxylic acid ligand. Indeed a carboxylate ligand may serve as a convenient conduit for delivering a proton to a bound peroxide in order to facilitate O-O bond cleavage, for example, in the conversion of intermediate **P** to **Q** in the case of sMMO for which a proton is clearly implicated.[13,55]

Supplementary Material

Refer to Web version on PubMed Central for supplementary material.

Acknowledgments

This work was supported by the National Institutes of Health (GM-38767 to L.Q.) and the Department of Energy (DE-FG02-06ER15799 to E.R.-A.); stopped-flow instrumentation at Tufts was supported by the NSF (CHE 0639138). We thank Dr. Victor Young, Jr. of the X-ray Crystallographic Laboratory at the University of Minnesota for his invaluable assistance.

References

1. Wallar BJ, Lipscomb JD. Chem Rev. 1996; 96:2625. [PubMed: 11848839]
2. Que, L, Jr. Bioinorganic Catalysis. 2. Reedijk, J.; Bouwman, E., editors. Marcel Dekker; New York: 1999. p. 269
3. Solomon EI, Brunold TC, Davis MI, Kemsley JN, Lee SK, Lehnert N, Neese F, Skulan AJ, Yang YS, Zhou J. Chem Rev. 2000; 100:235. [PubMed: 11749238]
4. Merkx M, Kopp DA, Sazinsky MH, Blazyk JL, Müller J, Lippard SJ. Angew Chem Int Ed. 2001; 40:2782.
5. Fox BG, Lyle KS, Rogge CE. Acc Chem Res. 2004; 37:421. [PubMed: 15260504]
6. Bollinger JM Jr, Diao Y, Matthews ML, Xing G, Krebs C. Dalton Trans. 2009:905. [PubMed: 19173070]
7. Sazinsky MH, Lippard SJ. Acc Chem Res. 2006; 39:558. [PubMed: 16906752]
8. Murray LJ, Lippard SJ. Acc Chem Res. 2007; 40:466. [PubMed: 17518435]
9. Liu KE, Valentine AM, Qiu D, Edmondson DE, Appelman EH, Spiro TG, Lippard SJ. J Am Chem Soc. 1995; 117:4997.
10. Bollinger JM Jr, Krebs C, Vicol A, Chen S, Ley BA, Edmondson DE, Huynh BH. J Am Chem Soc. 1998; 120:1094.

11. Broadwater JA, Ai J, Loehr TM, Sanders-Loehr J, Fox BG. Biochemistry. 1998; 37:14664. [PubMed: 9778341]
12. Broadwater JA, Achim C, Münck E, Fox BG. Biochemistry. 1999:12197. [PubMed: 10493786]
13. Lee SK, Lipscomb JD. Biochemistry. 1999; 38:4423. [PubMed: 10194363]
14. Saleh L, Krebs C, Ley BA, Naik S, Huynh BH, Bollinger JM. Biochemistry. 2004; 43:5953. [PubMed: 15147179]
15. Murray LJ, Garcia-Serres R, Naik S, Huynh BH, Lippard SJ. J Am Chem Soc. 2006; 128:7458. [PubMed: 16756297]
16. Yun D, Garcia-Serres R, Chicalese BM, An YH, Huynh BH, Bollinger JM Jr. Biochemistry. 2007; 46:1925. [PubMed: 17256972]
17. Vu VV, Emerson JP, Martinho M, Kim YS, Münck E, Park MH, Que JL. Proc Nat Acad Sci. 2009; 106:14814. [PubMed: 19706422]
18. Tshuva EY, Lippard SJ. Chem Rev. 2004; 104:987. [PubMed: 14871147]
19. Ookubo T, Sugimoto H, Nagayama T, Masuda H, Sato T, Tanaka K, Maeda Y, Okawa H, Hayashi Y, Uehara A, Suzuki M. J Am Chem Soc. 1996; 118:701.
20. Dong Y, Yan S, Young VG Jr, Que L Jr. Angew Chem Int Ed Engl. 1996; 35:618.
21. Kim K, Lippard SJ. J Am Chem Soc. 1996; 118:4914.
22. Zhang X, Furutachi H, Fujinami S, Nagatomo S, Maeda Y, Watanabe Y, Kitagawa T, Suzuki M. J Am Chem Soc. 2005; 127:826. [PubMed: 15656607]
23. Kryatov SV, Chavez FA, Reynolds AM, Rybak-Akimova EV, Que L Jr, Tolman WB. Inorg Chem. 2004; 43:2141. [PubMed: 15018538]
24. Korendovych IV, Kryatov SV, Reiff WM, Rybak-Akimova EV. Inorg Chem. 2005; 44:8656. [PubMed: 16296818]
25. Kryatov SV, Taktak S, Korendovych IV, Rybak-Akimova EV, Kaizer J, Torelli S, Shan X, Mandal S, MacMurdo V, Mairata i Payeras A, Que L Jr. Inorg Chem. 2005; 44:85. [PubMed: 15627364]
26. Yoon S, Lippard SJ. Inorg Chem. 2006; 45:5438. [PubMed: 16813407]
27. Fiedler AT, Shan X, Mehn MP, Kaizer J, Torelli S, Frisch JR, Kodera M, Que L Jr. J Phys Chem A. 2008; 112:13037. [PubMed: 18811130]
28. Frisch JR, Vu VV, Martinho M, Münck E, Que L Jr. Inorg Chem. 2009; 48:8325. [PubMed: 19610611]
29. Ménage S, Brennan BA, Juarez-Garcia C, Münck E, Que L Jr. J Am Chem Soc. 1990; 112:6423.
30. Rardin RL, Tolman WB, Lippard SJ. New J Chem. 1991; 15:417.
31. McKee V, Zvagulis M, Dagdigian JV, Patch MG, Reed CA. J Am Chem Soc. 1984; 106:4765.
32. Armarego, WLF.; Perrin, DD. Purification of Laboratory Chemicals. Butterworth-Heinemann; Oxford: 1997.
33. Hagen KS. Inorg Chem. 2000; 39:5867. [PubMed: 11151391]
34. Kryatov SV, Rybak-Akimova EV, Schindler S. Chem Rev. 2005; 105:2175. [PubMed: 15941212]
35. Bruker. SMART V5.054. Bruker Analytical X-Ray Systems; Madison, WI: 2001.
36. Blessing RH. Acta Cryst. 1995; A51:33.
37. Bruker. SAINT+ V6.45. Bruker Analytical X-Ray Systems; Madison, WI: 2003.
38. Bruker. SHELXTL V6.14. Bruker Analytical X-Ray Systems; Madison, WI: 2000.
39. Spek, AL. PLATON A multipurpose crystallographic tool. Utrecht University; Utrecht, The Netherlands: 2002.
40. Addison AW, Rao TN, Reedijk J, Rijn Jv, Verschoor GC. J Chem Soc, Dalton Trans. 1984:1349.
41. Yan S, Cheng P, Wang Q, Liao D, Jiang Z, Wang G. Science in China, Series B: Chemistry. 2000; 43:405.
42. Dong Y, Ménage S, Brennan BA, Elgren TE, Jang HG, Pearce LL, Que L Jr. J Am Chem Soc. 1993; 115:1851.
43. Feig AL, Becker M, Schindler S, van Eldik R, Lippard SJ. Inorg Chem. 1996; 35:2590. [PubMed: 11666474]
44. Feig AL, Lippard SJ. J Am Chem Soc. 1994; 116:8410.

45. Korendovych IV, Kryatov SV, Rybak-Akimova EV. Acc Chem Res. 2007; 40:510. [PubMed: 17521158]
46. Costas M, Cady CW, Kryatov SV, Ray M, Ryan MJ, Rybak-Akimova EV, Que L Jr. Inorg Chem. 2003; 42:7519. [PubMed: 14606847]
47. Than R, Schrodt A, Westerheide L, Eldik Rv, Krebs B. Eur J Inorg Chem. 1999:1537.
48. Lide, DR. CRC Handbook of Chemistry and Physics. 72. CRC Press; Boston: 1991.
49. Kilpatrick ML, Fackenthal E. Journal of the Electrochemical Society. 1953; 100:185.
50. Sergeant, EP.; Dempsey, B. Ionisation Constants of Organic Acids. Pergamon Press; New York: 1979.
51. Kilpatrick ML. J Am Chem Soc. 1949; 71:2607.
52. Shin TW, Kim K, Lee IJ. J Sol Chem. 1997; 26:379.
53. Edmundson, RS. Dictionary of Organophosphorus Compounds. Chapman and Hall; New York: 1988.
54. Do LH, Hayashi T, Moënne-Loccoz P, Lippard SJ. J Am Chem Soc. 2010; 132:1273. [PubMed: 20055391]
55. Tinberg CE, Lippard SJ. Biochemistry. 2009; 48:12145. [PubMed: 19921958]

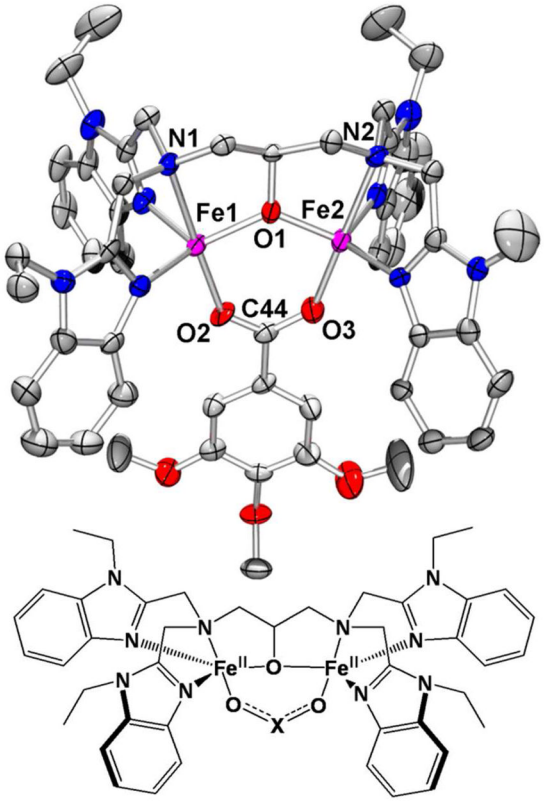

Figure 1.

Crystal structure of the cation **1**•$O_2CC_6H_2$-3,4,5-$(OMe)_3$ (50% ellipsoids) with hydrogen atoms removed. Generic cartoon of **1**•O_2X: O_2X = O_2AsMe_2 (**1**•O_2AsMe_2), O_2PPh_2 (**1**•O_2PPh_2), O_2PMe_2 (**1**•O_2PMe_2), $O_2P(OPh)_2$ (**1**•$O_2P(OPh)_2$), $O_2CC_6H_2$-3,4,5-$(OMe)_3$ (**1**•$O_2CC_6H_2$-3,4,5-$(OMe)_3$), O_2CPh (**1**•O_2CPh).

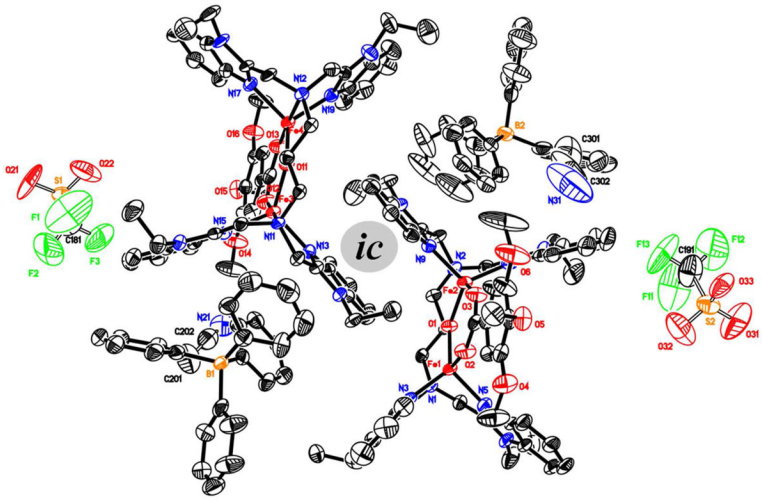

Figure 2.

ORTEP diagram (50% ellipsoids) of the unit cell containing two molecules of $[Fe_2(N\text{-}EtHPTB)(O_2CC_6H_2\text{-}3,4,5\text{-}(OMe)_3)]^{2+}$ and accompanying anions and solvent molecules (hydrogen atoms removed for clarity). There is a pseudo-inversion center (*ic*) between the cations. Comparing the cations, we find that the “inversion” is almost true, whereas comparing the BPh_4 ions reveals differences in thermal ellipsoid size and minor differences in atom locations, indicating that the inversion center is not real.

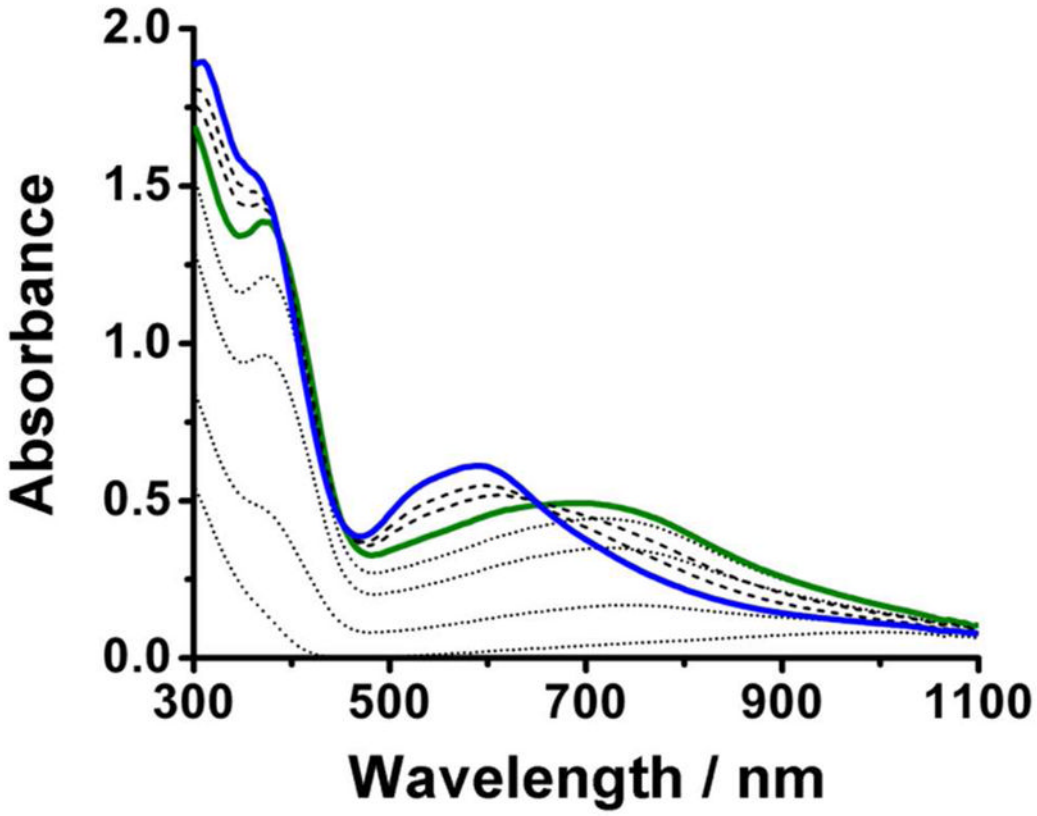

Figure 3.

Selected UV-Vis spectra obtained in the reaction of O_2 and **1**•O_2CCPh_3 in CH_2Cl_2 at −90° showing initial formation of **2**•O_2CCPh_3 (solid green line) and subsequent conversion to **3**•O_2CCPh_3 (solid blue line). Dotted lines correspond to spectra leading to the appearance of **2**•O_2CCPh_3 within the first 40 seconds, while dashed lines correspond to spectra associated with the conversion of **2**•O_2CCPh_3 to **3**•O_2CCPh_3 over the course of the following hour.

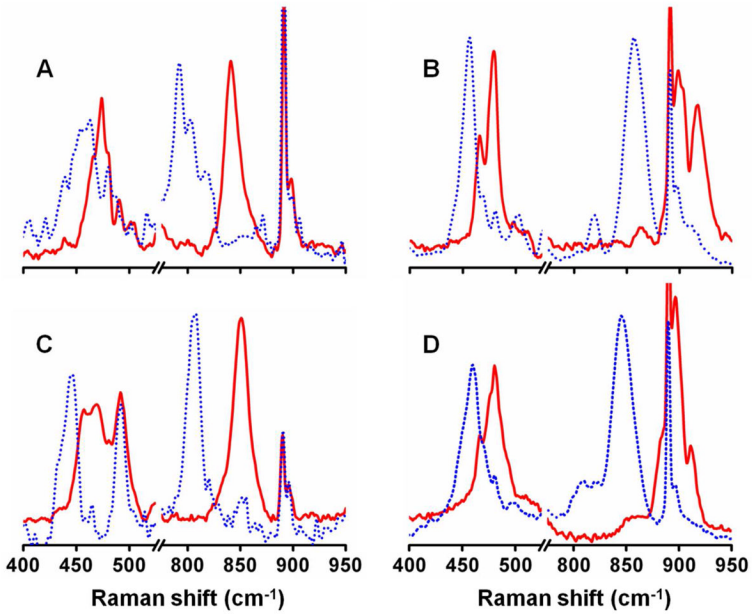

Figure 4.

Resonance Raman spectra of **2**•O_2CCPh_3 (**A**), **3**•O_2CCPh_3 (**B**), **2**•$O_2P(OPh)_2$ (**C**) and **3**•$O_2P(OPh)_2$ (**D**). Solid red lines ($^{16}O_2$) and dotted blue lines ($^{18}O_2$); T = 77 K, λ_{ex} = 647 nm.

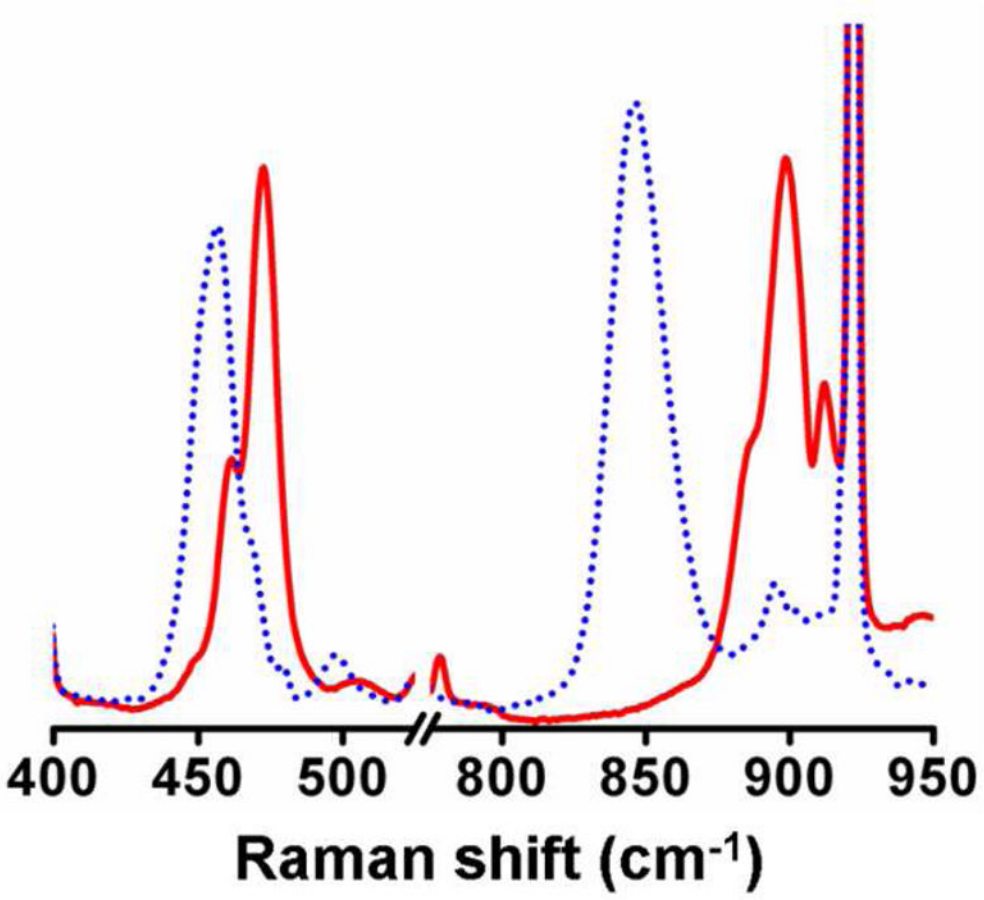

Figure 5.
Resonance Raman spectra of **3′**•O_2PPh^2 ($^{16}O_2$ = solid red line, $^{18}O_2$ = dotted blue line).

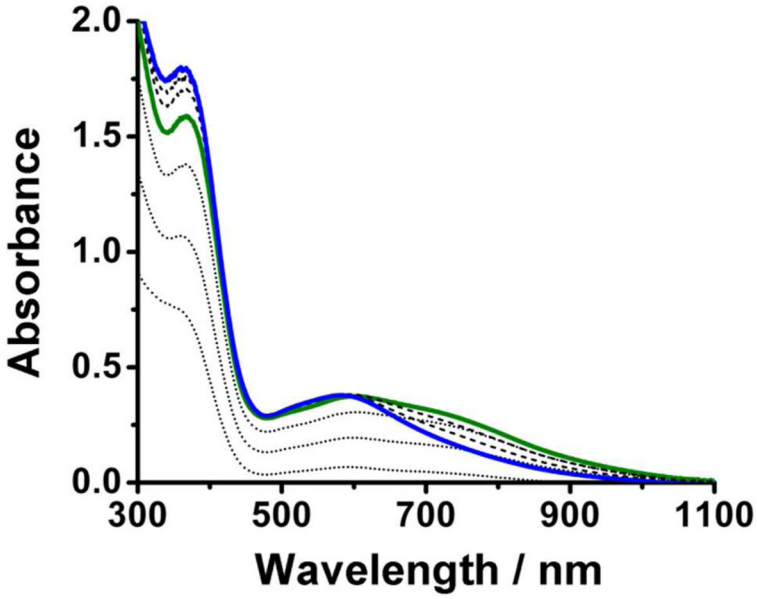

Figure 6.

Selected UV-Vis spectra obtained in the reaction of O_2 with **1**•O_2CPh at −90° showing evidence for the formation of two peroxo intermediates. The solid green line represents the spectrum with the largest fraction of **2**•O_2CPh formed, while the solid blue line corresponds to the subsequently formed **3**•O_2CPh. Dotted lines correspond to spectra leading to the maximum amount of **2**•O_2CPh formed within the first 90 seconds after oxygenation, while dashed lines correspond to spectra associated with the conversion of **2**•O_2CPh to **3**•O_2CPh over the course of the following 30 minutes.

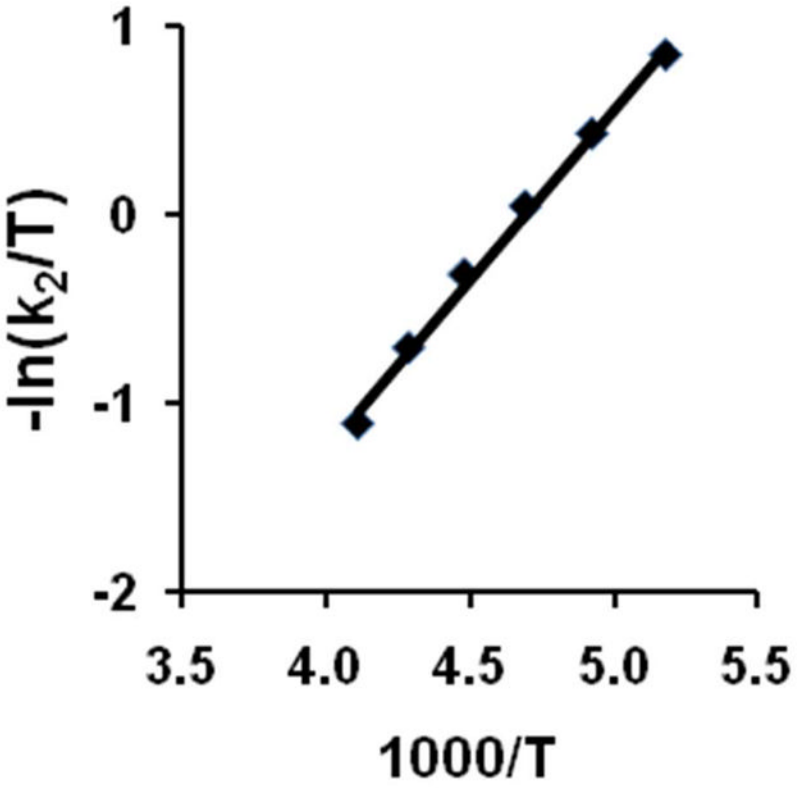

Figure 7.
Eyring plot for O_2 binding to **1**•O_2PPh_2 in CH_2Cl_2.

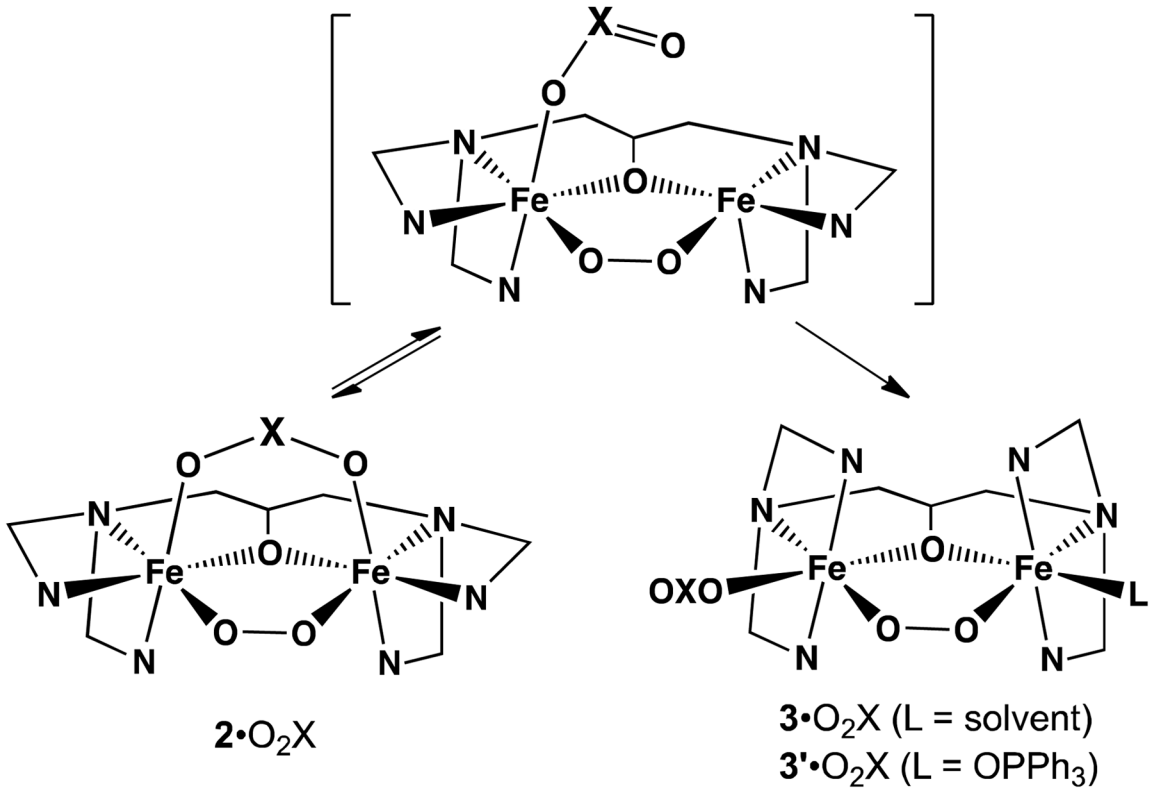

Scheme 1.
Conversion of **2**•O_2X to **3**•O_2X or **3**′•O_2X.

Table 1

Crystal data and structure refinement for **1**•$O_2PMe_2(BPh_4)(OTf)$•MeCN, **1**•$O_2P(OPh)_2(BPh_4)_2$•MeCN, and (**1**•$O_2CC_6H_2$-3,4,5-$(OMe)_3)_2(BPh_4)_2(OTf)_2$•2MeCN

	[1•O_2PMe_2]-(BPh_4)(OTf)•MeCN	**[1•$O_2P(OPh)_2$]-$(BPh_4)_2$•MeCN**	**[1•$O_2CC_6H_2$-3,4,5-$(OMe)_3]_2(BPh_4)_2(OTf)_2$-•2MeCN**
empirical formula	$C_{72}H_{78}BF_3Fe_2N_{11}O_6PS$	$C_{105}H_{102}B_2Fe_2N_{11}O_5P$	$C_{160}H_{166}B_2F_6Fe_4N_{22}O_{18}S_2$
fw	1435.99	1762.27	3108.29
T(K)	173(2)	173(2)	173(2)
Mo Kα λ, Å	0.71073	0.71073	0.71073
space group	$P2_1/c$	$P2_1/n$	P-1
a (Å)	16.0709(9)	23.063(4)	12.576(4)
b (Å)	15.6360(9)	18.942(4)	19.153(7)
c (Å)	28.4703(15)	23.888(4)	36.053(12)
α (deg)	90	90	96.743(5)
β (deg)	103.5800(10)	99.205(3)	92.147(5)
γ (deg)	90	90	103.100(5)
V (Å^3)	6954.1(7)	10301(3)	8381(5)
Z	4	4	2
ρ (calc), Mg/m^3	1.372	1.136	1.232
abs coeff (mm^{-1})	0.539	0.352	0.437
R1[a]	0.0398	0.0446	0.0713
wR2[b]	0.0984	0.1271	0.1955

[a] $R1 = \Sigma||F_O|-|F_C||/\Sigma|F_O|$.

[b] $wR2 = [\Sigma[w(F_O^2-F_C^2)2]/\Sigma\ [w(F_O^2)^2]]^{1/2}$.

Table 2

Selected interatom distances and bond angles for $[Fe_2(N\text{-}EtHPTB)(O_2X)]^{2+}$.

	1•O_2AsMe_2[a]	**1•O_2PPh_2**[a]	**1•O_2PMe_2**	**1•$O_2P(OPh)_2$**	**1•$O_2CC_6H_2$-3,4,5-$(OMe)_3$**[b]	**1•O_2CPh**[a]
τ_{ave}	0.81	0.77	0.82	0.91	0.89	0.93
Interatom distances (Å)						
Fe1-O1	2.0145(13)	2.004(2)	2.0184(18)	2.0057(16)	1.967(3)	1.976(5)
Fe2-O1	2.0037(14)	1.992(2)	1.9995(18)	2.0031(15)	1.970(3)	1.964(5)
Fe1-N1	2.3366(16)	2.294(3)	2.323(2)	2.3141(18)	2.328(4)	2.316(6)
Fe2-N2	2.3892(16)	2.352(3)	2.372(2)	2.309(2)	2.314(4)	2.280(7)
Fe1-O2	1.9825(14)	2.008(2)	2.0037(19)	2.0562(16)	2.036(3)	2.057(5)
Fe2-O3	1.9863(14)	2.021(2)	2.0123(18)	2.0506(16)	2.025(3)	2.019(6)
Fe1-N3	2.1372(17)	2.086(3)	2.105(2)	2.0668(19)	2.045(4)	2.064(6)
Fe1-N5	2.1023(18)	2.115(3)	2.127(2)	2.0732(19)	2.046(4)	2.069(6)
Fe2-N7	2.1088(17)	2.075(3)	2.098(2)	2.0551(19)	2.063(4)	2.080(6)
Fe2-N9	2.0759(17)	2.098(3)	2.080(2)	2.075(2)	2.044(4)	2.064(6)
As1/P1/C44-O2	1.6740(15)	1.514(2)	1.509(2)	1.4762(17)	1.254(5)	1.264(9)
As1/P1/C44-O3	1.6776(14)	1.512(2)	1.517(2)	1.4784(18)	1.273(5)	1.253(9)
Fe1···Fe2	3.5357(5)	3.5405(10)	3.5364(6)	3.6211(7)	3.4879(13)	3.4749(31)
O2···O3	2.7991(21)	2.5600(32)	2.5545(28)	2.5520(24)	2.2253(46)	2.2251(74)
Bond angles (degrees)						
Fe1-O1-Fe2	123.27(6)	124.76(11)	123.32(9)	129.19(8)	124.73(15)	123.8(2)
O1-Fe1-O2	105.77(6)	105.55(9)	102.50(8)	98.99(6)	98.27(13)	98.6(2)
O1-Fe2-O3	107.92(6)	99.44(9)	103.98(8)	98.93(7)	100.51(13)	101.5(2)
Fe1-O2-As1/P1/C44	127.24(8)	132.01(14)	131.47(12)	133.92(11)	138.1(3)	136.4(5)
Fe2-O3-As1/P1/C44	128.15(8)	138.88(15)	132.54(12)	133.24(10)	134.7(3)	133.9(5)
O2-As1/P1/C44-O3	113.26(7)	115.59(13)	115.17(12)	119.47(10)	123.4(4)	124.2(7)

[a] Data from reference 28.

[b] The unit cell of this compound contains virtual twins of **1**•$O_2CC_6H_2$-3,4,5-$(OMe)_3$ produced through a pseudo-inversion center. As there is no substantive difference between the two cations, values listed here are taken from a single cation.

Table 3

UV-Vis properties of **2**•O_2X, **3**•O_2X and **3′**•O_2X in CH_2Cl_2.

O_2X	λ_{max} (nm), [ε] (M^{-1} cm^{-1})		
	2•O_2X	**3**•O_2X	**3′**•O_2X
O_2AsMe_2	632 [2100]	-- [a]	-- [b]
O_2PMe_2	674 [1800]	-- [a]	616 [2400]
O_2PPh_2	678 [2100]	621 [1800]	592 [2600]
$O_2P(OPh)_2$	680 [2800]	576 [3100]	594 [3600]
O_2CCPh_3	708 [2500]	630 [2200]	595 [3300]
O_2CCMe_3	706 [--] [c]	580 [3100]	577 [3800]
O_2CPh	704 [--][c]	588 [1500][d]	592 [2300]
$O_2CC_6H_2$-3,4,5-$(OMe)_3$	707 [2600]	590 [3200]	592 [4300]
$O_2CC_6H_3$-3,4-$(OMe)_2$	704 [--][c]	578 [6200]	590 [5300]
$O_2CC_6H_3$-3,5-$(OMe)_2$	706 [--][c]	588 [5400]	592 [5600]
$O_2CC_6H_4$-4-OMe	705 [--][c]	580 [3000]	590 [4000]

[a] Conversion to **3**•O_2X did not take place at any temperature.

[b] Conversion to **3′**•O_2X did not take place at any temperature even with addition of 100 equivalents of $OPPh_3$.

[c] Conversion of **2**•O_2X to **3**•O_2X began before complete formation of **2**•O_2X, so ε was not determined.

[d] Values from reference 42.

Table 4

Fe–O and O–O stretching frequencies of **2**•O_2X and **3**•O_2X complexes determined using resonance Raman spectroscopy.

O_2X	**2**•O_2X		**3**•O_2X	
	$\nu_{Fe\text{-}O}$ (cm^{-1}) [^{18}O]	$\nu_{O\text{-}O}$ (cm^{-1}) [$^{18}O_2$]	$\nu_{Fe\text{-}O}$ (cm^{-1}) [^{18}O]	$\nu_{O\text{-}O}$ (cm^{-1}) [$^{18}O_2$]
O_2AsMe_2	464 [433]	845 [796]	--	--
O_2PMe_2	467, 479 [449, 460]	839 [791]	--	--
O_2PPh_2	465, 476 [455]	845, 853 [807]	477 [458]	897 [848]
$O_2P(OPh)_2$	457, 469 [436, 446]	851 [806]	479 [460]	897 [845]
O_2CCPh_3	466, 474 [447, 454]	841 [792]	466, 479 [448, 456]	903, 917 [857]
O_2CCMe_3	--	--	466, 475 [447, 457]	897, 912 [846]
O_2CPh[a]	--	--	476 [460]	900 [850]
$O_2CC_6H_2$-3,4,5-$(OMe)_3$	--	--	465, 476 [449, 457]	900, 914 [853]
$O_2CC_6H_3$-3,4-$(OMe)_2$	--	--	466, 474 [449, 456]	898, 912 [847]
$O_2CC_6H_3$-3,5-$(OMe)_2$	--	--	465, 476 [449, 458]	899, 913 [848]
$O_2CC_6H_4$-4-OMe	--	--	466, 474 [448, 457]	899, 913 [847]

[a]Values from reference 42.

Table 5

pK_a values of HO_2X and first order k_{obs} values for conversion of **2**•O_2X to **3**•O_2X and **2**•O_2X to **3′**•′ O_2X.

O_2X	pK_a of HO_2X	**2** → **3** [a] K_{obs} (s^{-1})	**2** → **3′** [b] K_{obs} (s^{-1})
O_2AsMe_2	6.27	-- [c]	-- [d]
O_2PMe_2	3.08 [e]	-- [c]	$1.8(4) \times 10^{-4}$ (−40 °C)
O_2PPh_2	2.32 [e]	3.1×10^{-4} [f] (−40 °C)	$4.3(4) \times 10^{-3}$ (−40 °C)
$O_2P(OPh)_2$	1.85 [e]	$1.2(1) \times 10^{-4}$	$3.1(1) \times 10^{-2}$
$O_2CC_6H_2$-3,4,5-$(OMe)_3$	4.24	$4.2(6) \times 10^{-4}$	0.13(5)
$O_2CC_6H_3$-3,4-$(OMe)_2$	4.36	$6.6(9) \times 10^{-4}$	0.12(1)
O_2CCPh_3	3.96	$1.7(2) \times 10^{-3}$	$2.6(3) \times 10^{-2}$
$O_2CC_6H_3$-3,5-$(OMe)_2$	3.97	$4.8(2) \times 10^{-3}$	0.20(1)
$O_2CC_6H_4$-4-OMe	4.50	$4.7(4) \times 10^{-3}$	0.12(1)
O_2CCMe_3	5.03	$1.8(1) \times 10^{-2}$	$8.0(3) \times 10^{-2}$
O_2CPh	4.19	$5.3(1) \times 10^{-2}$ [g] (−80 °C)	-- [h]

[a] All rates measured at −90 °C except where noted.

[b] All rates measured after addition of 20 equivalents of $OPPh_3$ at −90 °C except where noted.

[c] Conversion to **3**•O_2X did not take place at any temperature.

[d] Conversion to **3′**•O_2X did not take place at any temperature even with addition of 100 equivalents of $OPPh_3$.

[e] Measured in 7% EtOH (Reference 53).

[f] t −40 °C in CH_2Cl_2, **3**•O_2PPh_2 starts to decay before complete conversion from **2**•O_2PPh_2 occurs. For this reason, k_{obs} was calculated from the y-intercept of the $OPPh_3$ concentration dependence plot for the conversion of **2**•O_2PPh_2 to **3′**•O_2PPh_2 (Figure S2).

[g] Rate measured at −80 °C using stopped-flow techniques.

[h] By the time enough **2**•O_2CPh had formed to allow for addition of $OPPh_3$, significant conversion to **3**•O_2CPh had occurred, preventing accurate rate determination for the conversion of **2**•O_2CPh to **3′**•O_2CPh.

Table 6

Kinetic parameters for reactions of diiron(II) complexes with dioxygen

Complex	Solvent	*T* range (°C)	*K* (−40 °C) (M^{-1} s^{-1})	$\Delta H^{\ddagger}$ (kJ/mol)	$\Delta S^{\ddagger}$ (J/K·mol)	Reference
1•O_2PPh_2	CH_2Cl_2	−80 to −20	4.7×10^2	15.7(4)	−124(6)	This work
1•O_2PPh_2	MeCN	−40 to 0	2.55×10^3	13.7(4)	−119(10)	This work
1•O_2CPh	EtCN	−75 to −15	$1.03(12)\times10^2$	15.4(6)	−121(3)	43
$[Fe_2(HPTP)(O_2CPh)]^{2+}$	MeCN	−40 to 0	7.3×10^3	15.8(4)	−101(10)	46
$[Fe_2(HPTP)(O_2CPh)]^{2+}$	CH_2Cl_2	−80 to 0	67	16.7(2)	−132(8)	46